



HAL
open science

Measurements of profiles of the wavefront outer scale using observations of the limb of the Moon

J. Maire, A. Ziad, J. Borgnino, F. Martin

► **To cite this version:**

J. Maire, A. Ziad, J. Borgnino, F. Martin. Measurements of profiles of the wavefront outer scale using observations of the limb of the Moon. *Monthly Notices of the Royal Astronomical Society*, 2007, 377, pp.1236-1244. hal-00417123

HAL Id: hal-00417123

<https://hal.science/hal-00417123>

Submitted on 19 Nov 2021

HAL is a multi-disciplinary open access archive for the deposit and dissemination of scientific research documents, whether they are published or not. The documents may come from teaching and research institutions in France or abroad, or from public or private research centers.

L'archive ouverte pluridisciplinaire **HAL**, est destinée au dépôt et à la diffusion de documents scientifiques de niveau recherche, publiés ou non, émanant des établissements d'enseignement et de recherche français ou étrangers, des laboratoires publics ou privés.



Distributed under a Creative Commons Attribution 4.0 International License

Measurements of profiles of the wavefront outer scale using observations of the limb of the Moon

J. Maire,[★] A. Ziad, J. Borgnino and F. Martin

Université de Nice-Sophia-Antipolis, UFR Sciences, Lab. Univ. d'Astrophysique de Nice (LUAN) UMR 6525, Parc Valrose, F-06108 Nice Cedex 2, France

Accepted 2007 February 27. Received 2007 February 26; in original form 2006 July 14

ABSTRACT

The wavefront outer scale is an important parameter to use when evaluating the experimental performance of large aperture telescopes. Knowledge of three-dimensional atmospheric wavefront distortions is required for specifications of multiconjugate adaptive optics systems, which are essential for observations using Extremely Large Telescopes with a wider field of view. We aim to estimate the vertical distribution of the wavefront outer scale. We analyse the angular correlation of the fluctuations of the wavefront angle of arrival, deduced from image motion of the limb of the Moon. We use a simulated annealing algorithm to deduce the height dependence of the wavefront outer scale with given C_N^2 profiles simultaneously measured with the scintillation detection and ranging (SCIDAR) instrument. We present results obtained during two campaigns of observation at the Mauna Kea Observatory (Hawaii) and the Observatoire de Haute Provence (France). Estimated profiles of the outer scale exhibit smaller values in the boundary layer than in the free atmosphere. Comparisons with measurements of the outer scale using the Generalized Seeing Monitor (GSM) are possible and give good agreement. We consider some implications for adaptive optics systems.

Key words: atmospheric effects – instrumentation: adaptive optics.

1 INTRODUCTION

Astronomical images produced by a ground-based telescope are severely degraded by wavefront atmospheric propagation. Knowledge of wavefront fluctuations is very important for the design of the next generation of Extremely Large Telescopes (ELTs) and long-baseline interferometers. With this knowledge it is possible to specify the basic parameters of these instruments and their subsystems, such as adaptive optics systems, wavefront tip-tilt correctors and fringe trackers, which overcome the limitations imposed by the atmosphere.

The performance and optimization of such systems are related to atmospheric conditions and notably to the amplitude of the wavefront outer scale, which gives an estimation of the spatial coherence and spatial correlation of the wavefront at large scales. This is an important parameter that influences several topics in astronomy, such as diffraction-limited cores in uncorrected images, astrometric accuracy, the stroke of deformable mirrors and interferometer operations.

The Generalized Seeing Monitor (GSM) instrument is dedicated to measurements of this outer scale (Martin et al. 1994), and several site-testing campaigns have been carried out worldwide (Ziad et al. 2000). Measurements of the outer scale have been confirmed by processing data obtained with existing high angular resolution

instruments such as optical interferometers (Ziad et al. 2004; Maire et al. 2006) and adaptive optics systems (Rigaut et al. 1991; Schöck et al. 2003; Fusco et al. 2004). However, there is limited knowledge about the properties and statistics of a large-scale wavefront. The model of turbulence must be statistically validated for decametric scales. A complete approach should consider wavefront perturbations arising from all turbulent layers located at different distances from the observer. Borgnino (1990) found a theoretical relation between height-dependent outer scales and those related to wavefront perturbations entering the pupils of telescopes.

Sky coverage limitations of an adaptive optics system as a result of anisoplanatism can be improved by techniques such as turbulence tomography and multiconjugate adaptive optics (Beckers 1988; Ragazzoni, Marchetti & Valente 2000), which retrieve three-dimensional instantaneous wavefront perturbations. The fluctuations of the air refractive index, as measured by the scintillation detection and ranging (SCIDAR) instrument, give information on the contribution of the different heights to the wavefront distortions. Spatial correlations on wavefront fluctuations at a large scale and related wavefront outer scale profiles are needed to complete the evaluation of atmospheric components that intervene in the optimal design of ELTs. For example, wavefront outer scale profiles are useful to define the maximal stroke needed for mirrors optically conjugated at different altitudes of the atmosphere.

We present a monitor of wavefront outer scale profiles (MOSP), which probes the correlations of the wavefront angle of arrival (AA) of the extent of the Moon's limb. In Section 2, we briefly review

[★]E-mail: jerome.maire@unice.fr

the theoretical background related to the angular correlations of the AA used to extract outer scale profiles. In Section 3, we detail the observations of the limb of the Moon, the experimental device used and the data processing. In Section 4, we present our results, and in Section 5 we consider some implications for adaptive optics systems. In Appendix A, we examine the relations between the height-dependent outer scale and the resulting outer scale measured at ground level, depending on the experimental conditions.

2 THEORETICAL BACKGROUND

Let us consider a plane wave with wavelength λ propagating downwards through the atmosphere, towards a ground-based observer. In a thin layer between h and $h + \delta h$, fluctuations in the air index, characterized by the structure constant C_N^2 , introduce fluctuations of phase shift ϕ . The phase power spectrum may be expressed by the von Kármán (vK) spectrum, which introduces the height-dependent wavefront outer scale $\mathcal{L}_0(h)$ (Borgnino, Martin & Ziad 1992)

$$W_\phi(f, h) = 0.38\lambda^{-2}C_N^2(h)\delta h \left[f^2 + \frac{1}{\mathcal{L}_0(h)^2} \right]^{-11/6}, \quad (1)$$

where f is the modulus of the spatial frequency f . The inner scale of the turbulence is assumed to be infinitely small and the turbulence is assumed to be isotropic, even at scales larger than the outer scale.

For geometrical optics, the AA is the normal to the wavefront at the observed point. The angular structure function $D_\alpha(\theta)$ of AA fluctuations α is defined as the mean-squared difference of the AA fluctuations observed in directions \mathbf{r} and $\mathbf{r} + \theta$, $D_\alpha(\theta) = \langle [\alpha(\mathbf{r}) - \alpha(\mathbf{r} + \theta)]^2 \rangle$, where the brackets $\langle \rangle$ denote an ensemble average. If the AA fluctuations are averaged over unobstructed circular apertures of diameter D , this angular structure function is obtained, taking account of a continuous distribution of turbulence (Borgnino et al. 1992; Avila et al. 1997; Bouzid et al. 2002) as

$$D_\alpha(\theta) = 2.4 \sec(z) \int_0^{+\infty} dh C_N^2(h) \int_0^{+\infty} df f^3 \times \left[f^2 + \frac{1}{\mathcal{L}_0(h)^2} \right]^{-11/6} F(f, h, \theta) G(f, D) H(f, h), \quad (2)$$

where z is the zenithal distance. The factor $F(f, h, \theta) = [1 - J_0(2\pi f\theta h) + \cos(2\gamma)J_2(2\pi f\theta h)]$ is the spatial frequency high-pass filter related to the different directions of observation or beam separation at altitude h , where J_n represents the n th-order Bessel function of the first kind. If AA fluctuations are observed perpendicular to the baseline B , the structure function is called transverse and $\gamma = \pi/2$ (Avila et al. 1997). The aperture filter function

$$G(f, D) = \left[\frac{2J_1(\pi Df)}{\pi Df} \right]^2$$

acts as a low-pass filter with a cut-off frequency that decreases with increasing D . The factor $H(f, h) = \cos^2(\pi\lambda h f^2)$, because of the Fresnel propagation, attenuates very high frequencies. The experiment proposed below measures the motion of the Moon's limb, which is considered as a distribution of incoherent point sources.

This structure function (equation 2), which gives an estimation of AA angular decorrelations, increases with the beam separation θ and becomes saturated for θh larger than $\mathcal{L}_0(h)$. Fig. 1 represents AA structure functions, for given altitude and outer scale, calculated from equation (2), with the value of C_N^2 at altitude h deduced from the Hufnagel profile (Voitikhovich et al. 1998, equation 7 with $C_0^2 = 1.229 \times 10^{-16} \text{ m}^{-2/3}$). It shows the effect of changing the value of the outer scale on the AA structure function. The AA angular

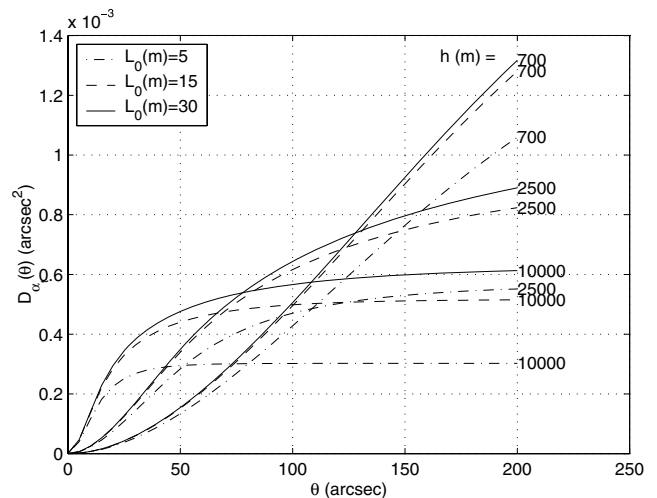


Figure 1. The AA transverse angular structure function deduced from equation (2), with $D = 0.6$ m and $\lambda = 0.5$ μm , for several values of the outer scale and for single layers (with altitudes labelled) with C_N^2 value at altitude h deduced from Hufnagel profile with $\delta h = 300$ m.

decorrelations are enhanced for small angular separations when the considered altitudes increase. For a given altitude, the saturation of the structure function appears at greater angular separation when the value of the outer scale increases.

The contribution to the seeing from different heights can be deduced by integrating $C_N^2(h)$. The Fried parameter r_0 depends physically on the structure constant of refractive index fluctuations $C_N^2(h)$ integrated along the propagation path (Roddier 1981) as

$$r_0 = \left[0.423 \left(\frac{2\pi}{\lambda} \right)^2 \sec(z) \int dh C_N^2(h) \right]^{-3/5}. \quad (3)$$

A turbulence distribution with altitude-dependent strength and outer scale can produce an integrated effect described by some average outer scale (see Appendix A).

3 EXPERIMENTAL DATA

3.1 Experimental device and observing campaigns

The telescope used during the Mauna Kea observing campaign was the 61-cm telescope of the University of Hawaii (UH), which has a 9.24-m Cassegrain focal length ($f/15.2$). For the Observatoire de Haute Provence (OHP) campaign, a 20-cm telescope ($f/15$) was used with a $\times 3$ diverging Barlow lens increasing the effective focal length of the system, thereby increasing the magnification of the instrument.

The optimal diameter of the telescope is a trade-off between the need to measure AA correlations in a large field of view and the angular resolution required for AA measurements. As there is a strong sensitivity of the AA structure function (equation 2) to the outer scale at large angular separation, we can consider a large field of view and a small diameter. However, the angular resolution, luminosity and magnification necessary tend to require a diameter in the range of 0.2–0.6 m for the instrumental set described here.

Images at the focal plane are recorded using a PixelFly CCD camera with 640×480 pixel matrix and $(9.9 \times 9.9) \mu\text{m}^2$ pixel size. The dynamic range of the analogue/digital conversion is 12 bits. The readout noise is 12 e- rms and the imaging frequency is 33 Hz.

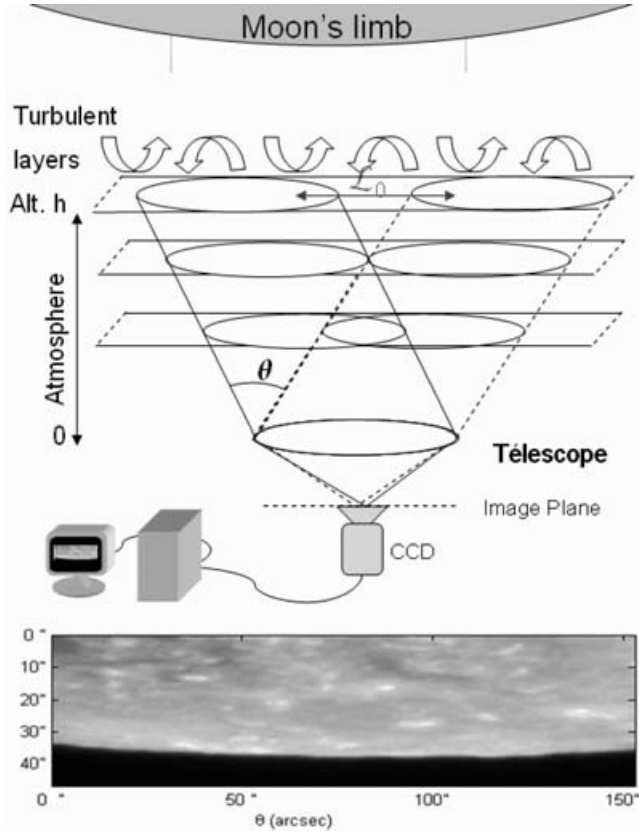


Figure 2. Experimental device and example of an 2-ms exposure image of the Moon limb observed with the UH 0.61-m telescope on 2005 July 17 at Mauna Kea. Axis units are in arcsec. The edge is detected and 2000 successive images are processed. θ is the angular beam separation.

In order to freeze atmospheric effects on the image motion of the Moon's limb, the exposure time was set to 1 or 2 ms. The spectral response of the camera is maximal for $\lambda = 0.5 \mu\text{m}$ in a 375–550 μm range. An example of the images obtained is given in Fig. 2 with an angular resolution of 0.22 arcsec per pixel. It can be seen in this figure that wavefronts arriving from two directions separated by an angle θ have a larger intersection at a low altitude; this gives more angular AA correlations on the image plane. At an altitude $h = D \cos(z)/\theta$, the two beams are disjointed but correlations are not loose until the altitude is high enough to have the two beams separated by a distance larger than $\mathcal{L}_0(h)$. We examine the recorded AA measurements in order to retrieve the optical wavefront parameters.

3.2 Data processing

The first step of data processing is to retrieve accurately the AA fluctuations from the motion of the Moon's limb. After processing on each image a flat and dark field correction, each image $I(x, y)$ is slightly blurred with a median filter M on 3×3 pixel blocks. This avoids possible outliers as a result of Poisson noise or the Moon's small features with relatively high intensity differences that can affect the detection of the limb. This type of filtering is more effective than convolution when the goal is to simultaneously reduce noise and preserve edges (Pratt 1978). Each output pixel with coordinates (x, y) contains the median value in the 3×3 neighbourhood around the corresponding pixel in the input image. Then, an image gradient

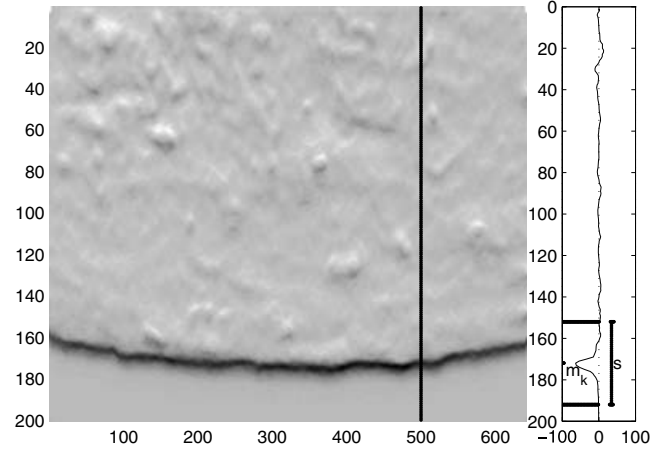


Figure 3. The Prewitt gradient of a short-exposure image of the limb of the Moon. Axis units are in pixels. The photocentre is detected on each column normal to the limb with a barycentric calculus of the photocentre in an extent s around the $\text{max } m_k$.

$G(x, y)$ is processed (Fig. 3) by convolution with a 3×3 Prewitt edge detector (Pratt 1978) defined as

$$P = \begin{pmatrix} -1 & -1 & -1 \\ 0 & 0 & 0 \\ 1 & 1 & 1 \end{pmatrix}$$

or $-P$ if the y -axis points to the centre of the Moon. Different edge detectors have been tested and the Prewitt edge detector appears to be more efficient (see below). Thus, the image gradient is defined as the convolution product $G(x, y) = P * M * I(x, y)$. When small apertures are used (i.e. in case of low photon flux level), the size of the neighbourhoods over which the differential gradients are computed should be extended. The detection of the limb position in absolute values of the image gradient is determined by a centroid calculation over columns k around each minimum at position m_k and with a window extent s . The centroid c_k is the position along each column normal to the edge extent, defined as

$$c_k = \frac{\sum_{j=m_k-s/2}^{j=m_k+s/2} jG(j, k)}{\sum_{j=m_k-s/2}^{j=m_k+s/2} G(j, k)}, \quad (4)$$

where the minimum at position m_k of the row gradient G_{ij} is taken as the centre of the window.

We process $N = 2000$ images (about 1 min of acquisition), which gives a set of limb angular positions obtained at time t . In order to retrieve transverse AA fluctuations α_{\perp} in a particular set of positions of the limb, we subtract from this set the temporal mean limb position obtained. The structure function of transverse AA fluctuation is calculated as

$$D_{\alpha_{\perp}}(\Theta) = \frac{1}{N} \sum_{i=1}^{i=N} \frac{1}{\Theta_m - \Theta} \sum_{k=1}^{k=\Theta_m - \Theta} [\alpha_{\perp}(k) - \alpha_{\perp}(k + \Theta)]^2 \quad (5)$$

where Θ is the angular separation in pixels and Θ_m is the maximal extent accessible in the image (i.e. 640 pixels in our case). This differential variance calculated for each image has the practical advantage of being insensitive to the vibration effects of the telescope and tracking errors.

This function and all the parameters deduced are scaled for the zenithal direction. Fig. 4 represents several AA transverse structure functions obtained at Mauna Kea on 2005 July 17. It is possible to

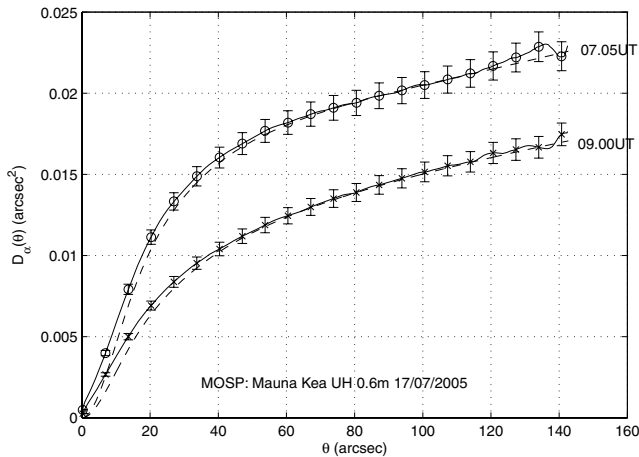


Figure 4. Examples of experimental structure functions of transverse AA fluctuations (solid line) obtained with 2000 successive images of the Moon’s limb during the night of 2005 July 17 with the UH 0.6-m telescope. A theoretical curve (dashed line) is fitted to each experimental curve. The error bars are calculated for each structure function by considering the precision of the AA measurements (see Section 3.3).

measure the AA angular correlation scale θ_c as the angular separation where the AA structure function reached e^{-1} of its saturation level. Our method can be affected by strong turbulence near the ground, which can give rise to an unsaturated AA structure function (see Fig. 1) in the angular extent considered. Ghedina, Ragazzoni & Baruffolo (1998) used a similar method to measure the isokinetic patch size on the edge of the Moon. As remarked by Belen’kii (2000) in the case of transverse Z-tilt, this correlation scale increases with the outer scale and with the telescope diameter. θ_c decreases as the optical strength located in the higher layers of the atmosphere increases (see Section 2).

Retrieving the profiles of $C_N^2(h)$ and $\mathcal{L}_0(h)$ from the AA structure functions (equation 2) is a non-linear inverse problem. We use a simulated annealing (SA) algorithm to minimize the cost function E , defined as the sum over the angular extent of the squared difference between measured and theoretical AA structure functions $E = \sum_{\theta} [D_{\alpha_1}(\theta) - D_{\alpha_r}(\theta)]^2$. This algorithm was developed to statistically find the best global fit of a non-linear non-convex cost function (Kirkpatrick, Gelatt & Vecchi 1983) and it has been recently used in the context of $C_N^2(h)$ measurements (Habib et al. 2006). Its name comes from thermodynamic statistics: when the temperature of a system of particles in interaction is cooled sufficiently slowly, the system reaches a minimal energy state. Each step of the SA algorithm replaces the current solution $[C_N^2(h); \mathcal{L}_0(h)]$ by a random ‘nearby’ solution, chosen with a probability that depends on the variations of the cost function and on a global parameter T (called temperature), which is gradually decreased during the process. The process is started with a given configuration $[C_N^2(h); \mathcal{L}_0(h)]$, and elementary random perturbation is applied to the current solution. If the cost decreases, the perturbation is accepted. If the cost increases, the perturbation is not systematically rejected but accepted with a probability $p = \exp(-\Delta E/T)$, where ΔE is the cost variation. This allowance saves the method from becoming stuck at local minima. In cases where $C_N^2(h)$ profiles are given by SCIDAR measurements, only $\mathcal{L}_0(h)$ are perturbed. At a given temperature, each component of the solution is iteratively perturbed until a statistical equilibrium is reached. Optimization is performed by gradually decreasing the temperature in order to converge to the optimal solution.

Several parameters of this method need to be adjusted. The initial temperature is chosen in order to have 80 per cent of accepted states when random perturbation is applied. For a given temperature, the statistical equilibrium is reached when the standard deviation of the cost function over a given number of iterations is practically constant. A proportional decreasing law of temperature is chosen as $T_{k+1} = aT_k$ with $a = 0.99$ (van Laarhoven & Aarts 1987; Aarts & Korst 1989). This is not the only possible cooling schedule but it is predominantly used. The system is considered sufficiently cooled when the cost function is lower than a value ϵ . This stop criterion is determined by testing the algorithm with synthetic data. This is a trade-off between the desired accuracy and the computing time constraint. The cost function gives a measure of the goodness of fit and the stop criterion of the SA algorithm ensures that a good fit has been reached for each file acquisition.

3.3 Error estimation

Owing to the high level of photon flux of the Moon, the exposure time (1 or 2 ms) is chosen to be short enough to freeze image motion completely and to keep a high signal-to-noise ratio. Indeed, the typical wavefront coherence time τ_0 is of the order of a few milliseconds (Roddier et al. 1990). The narrow spectral band, which is a result of the response of the CCD, has no significant effect on the differential and absolute image motion (Tokovinin 2002). The subtraction of the temporal mean limb position is needed to overcome the effect of the limb curvature when retrieving AA fluctuations. The fluctuations measured are not perfectly transverse to the limb on the image border (Fig. 2), that is, γ in equation (2) varies slightly over the limb extent. However, these variations are weak enough to be neglected given the maximal angular extent considered (140 arcsec for the Mauna Kea observations); the maximal variation is $\Delta\gamma = 4^\circ$, which gives a maximal variation lower than 0.1 per cent of the transverse AA structure function for all angular separations calculated using $\gamma = 90 \pm 4^\circ$ (equation 2). Given that the measured AA structure function for a given angular separation (equation 5) is averaged over the limb extent, the curvature effect can be neglected for all our measurements. For observations in a larger field of view, this effect should be considered as it yields up to 3 per cent of variations for a limb with an extent of 600 arcsec.

Conan et al. (2000b) found that both the theoretical and measured decorrelation times of AA fluctuations are of the order of 10 ms at La Silla. Assuming that temporal AA fluctuations are independent (imaging frequency of 33 Hz) and follow a Gaussian probability law, the statistical relative error in the calculation of AA differential variance depends on the angular separation considered (see equation 5). This is given by (Frieden 1983)

$$\frac{1}{2} \left[\frac{2}{N(\theta_{\max} + 1 - \theta) - 1} \right]^{1/2},$$

where N is the number of successive images per structure function obtained and θ is the angular separation in pixels. This gives a maximal statistical error of 1.5 per cent for 1 min of acquisition in the most unfavourable case of maximal angular separation measured.

The errors in measured limb position come from the noise in light intensities: the additive readout noise of the CCD and the Poisson noise of the signal itself. Tokovinin (2002) showed that the contribution of readout noise to image motion variance is inversely proportional to the square of the (stellar) flux. Typical photon counts per pixel are 1500 for a 2-ms short exposure image of the edge. We consider that the errors due to the readout noise given the high level of the Moon’s flux are negligible.

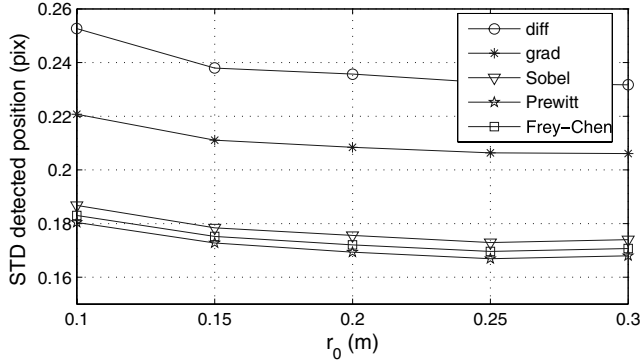


Figure 5. The simulated error position (rms) due to the photon noise effect on the detection of the Moon’s edge for several atmospheric conditions. Several edge detectors are compared; the Prewitt operator provides the best accuracy for detection, better than one-fifth of a pixel.

To estimate the effect of Poisson noise on measured position, we simulate images of the Moon’s limb for several seeing conditions. The atmospheric short-exposure two-dimensional (2D) transfer function (Korff 1973), the aperture transfer function and the Fourier transform of a 2D Heaviside function are multiplied in the Fourier plane. The 2D inverse Fourier transform gives a simulated Moon’s edge and intensities are scaled to correspond with the mean intensity measured in our images of the Moon. Poisson noise is added, input pixel values being interpreted as means of Poisson distributions. Then we applied methods of edge detection described above (median filtering and centroid windowing on a Prewitt gradient) to estimate the difference in position measured between initial and noisy images. This error and the standard deviation measured in fractions of pixels is averaged over the edge extent and given for several values of r_0 in Fig. 5. The detections of AA in these atmospheric conditions are always better than one-fifth of a pixel when the Prewitt gradient operator is used for edge detection. The best accuracy is obtained with the Prewitt operator rather than other edge detectors, such as the pixel difference, gradient, Sobel and Frei–Chen as defined by Pratt (1978). Considering α_{\perp} over the limb as an independent variable, the total differential of equation (5) is calculated for each angular separation, leading to the error in α_{\perp} . Given our angular resolution of 0.2 arcsec per pixel, this yields a maximal error of 3 per cent on the AA structure function (Fig. 4).

The resolution in altitude for the solution is chosen in order to have the same number of slices in the boundary layer and in the free atmosphere. We simulated AA structure functions with synthetic $C_N^2(h)$ and $\mathcal{L}_0(h)$ profiles in order to test the SA algorithm by comparing the results obtained. The results are more reliable when unknowns are only $\mathcal{L}_0(h)$. Noise is enhanced by inversion, especially when the resolution in altitude is high. Simulations with noisy synthetic data show that four layers in the first few kilometres of the atmosphere and three layers of 5–6 km thickness above give reliable results. The average difference between initial profiles of the outer scale and those obtained with the SA method is about 3 m per slice. Several resolutions in altitude for the atmosphere have been tested with several slices of equal thickness. Errors on $\mathcal{L}_0(h)$ increase with the number of slices, being less than 1 m per slice when four slices or fewer are used. Beyond eight slices, the errors become substantial. These errors increase considerably when C_N^2 and \mathcal{L}_0 need to be obtained simultaneously using the SA method. In this case, the optimal number of slices should not be greater than four in order to have errors on the outer scale of less than 5 m per slice.

4 RESULTS

A first observing campaign was performed at the OHP in France between 2004 November 24 and December 6. The site testing instruments GSM and SCIDAR were also observing simultaneously.

A second observation mission was carried out at the Mauna Kea Observatory in Hawaii between 2005 July 13 and 19 with simultaneous observations using the SCIDAR instrument installed at the UH 2.2-m telescope, 150 m north-east of the 0.61-m dome.

The GSM instrument measured the wavefront outer scale by measuring AA fluctuations at several points on the wavefront using four telescopes pointing at the same star. The outer scale \mathcal{L}_0 is determined for each pair of modules (six different baselines) by computing the ratio of AA covariance to the differential AA variance. These normalized covariances are then compared to a grid of theoretical covariances calculated with the vK model for different baseline coordinates and also for several values of \mathcal{L}_0 . The adopted \mathcal{L}_0 value is the median of the six obtained values. Ziad et al. (2000) have given a detailed description of the GSM instrument.

The generalized SCIDAR technique (Vernin & Roddier 1973; Fuchs, Tallon & Vernin 1998) is aimed at measuring C_N^2 profiles by analysing the spatial autocorrelation function of double star scintillation away from the pupil plane. The stars, separated by an angular distance θ , form two identical speckle patterns and give a peak in the autocorrelation function proportional to $C_N^2(h)$.

4.1 Profiles

First, we estimate both $C_N^2(h)$ and $\mathcal{L}_0(h)$ from the limb of the Moon. As the difference in altitude between the UH 0.6-m and the UH 2.2-m telescopes is about 30 m, a difference of total turbulent energy on the propagation path can occur. We increase the value of the SCIDAR C_N^2 in the lower slices until the C_N^2 integration over altitude corresponds to the initial integration of $C_N^2(h)$ estimated with the limb of the Moon. Secondly, these modified simultaneous SCIDAR C_N^2 profiles are used with the SA algorithm in order to have only $\mathcal{L}_0(h)$ as unknowns. The total error expected is about 10 per cent (see Section 3.3). The vertical resolution obtained is a trade-off between the need to have a good sample of the first kilometre above the observatory and the reliability expected for the results. The time series of wavefront outer scale profiles obtained at Mauna Kea are represented in Fig. 6. Examples of profiles obtained during the OHP and Mauna Kea campaigns are given in Fig. 7. The median profiles obtained during all the missions show lower values for the

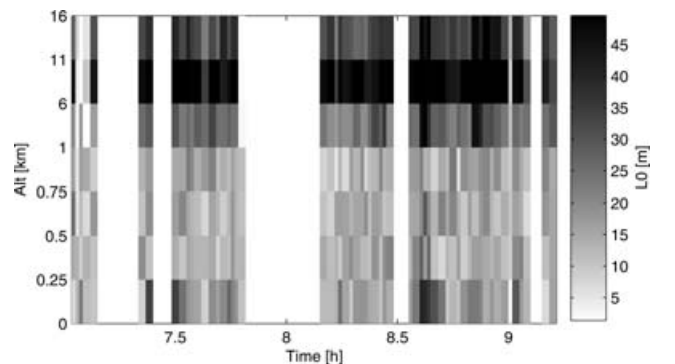


Figure 6. The height dependence of the outer scale measured at the Mauna Kea Observatory on the night of 2005 July 17. The altitude above the observatory is represented by a non-linear vertical axis. The C_N^2 profiles used were measured simultaneously by the SCIDAR instrument.

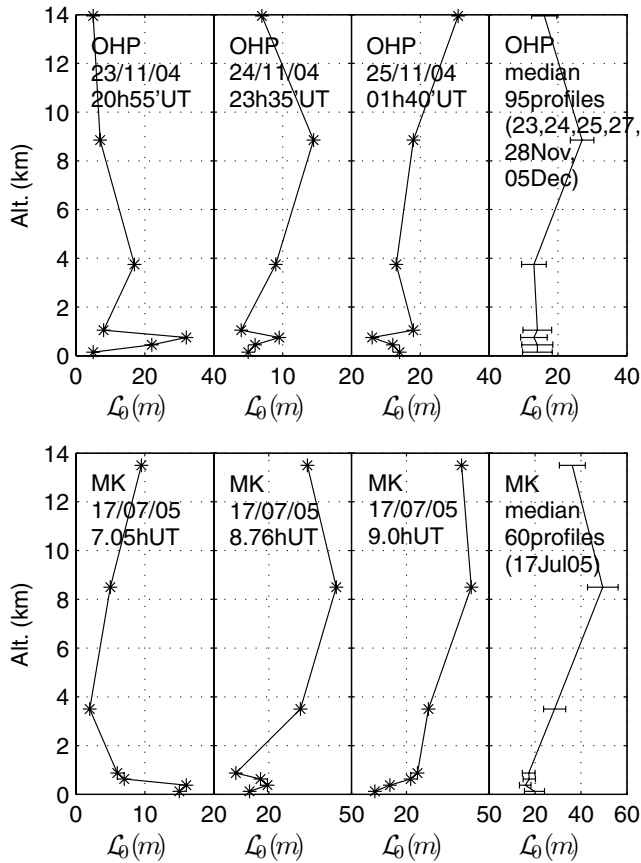


Figure 7. Examples of outer scale profiles obtained at the OHP (top) and the Mauna Kea Observatory (bottom) over several nights. Altitudes are those above the observatory. On the right, the median values of the outer scale for all the campaigns are represented with the standard deviation of the values obtained. The integrated outer scale (equation A4, $n = -1/3$) gives 14.0 m at the OHP and 26.9 m at Mauna Kea.

outer scale for the first kilometre of the atmosphere. These results can be completed with the theoretical relation found by Ishimaru (1978), who found that the outer scale is on the order of height near the ground.

It should be pointed that the SA algorithm is also appropriate to extract both $C_N^2(h)$ and $\mathcal{L}_0(h)$. In this case, the MOSP can be a completely independent instrument. However, the optimal vertical resolution in the free atmosphere is small compared to that of the SCIDAR instrument and the results obtained are less reliable. An example of the $C_N^2(h)$ profile obtained is compared with a simultaneous SCIDAR measurement and shows good agreement (Fig. 8).

4.2 Integrated results

The AA angular correlation scale is deduced directly from the AA structure function (see Section 3.2) and values estimated during the run of 2005 July 17 are presented in Fig. 9. The values obtained are very close to the results found by Ghedina et al. (1998). The tilt anisoplanatism angle (Sasiela & Shelton 1993) is defined as the angle between two beams at which the wavefront phase error as a result of the tilt anisoplanatism is 1 rad (Hardy 1998). This angle, calculated with SCIDAR C_N^2 profiles and an infinite outer scale, is

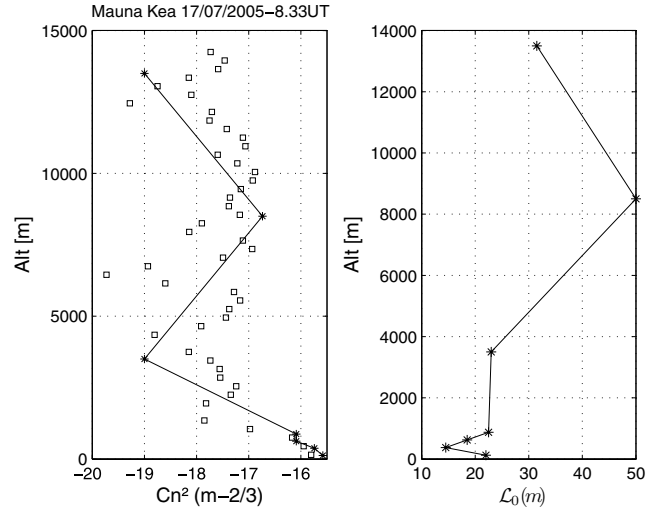


Figure 8. Example of C_N^2 and outer scale profiles (solid line) that can be retrieved simultaneously using the SA method. Comparisons with a simultaneous SCIDAR profile (squares) are in close agreement, despite the different vertical resolutions of these instruments.

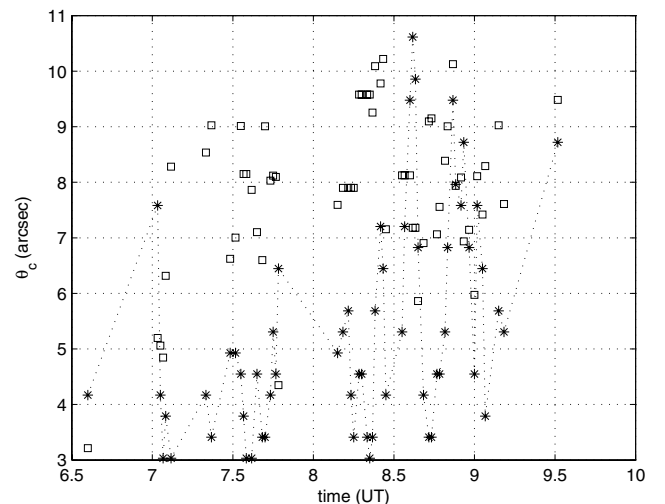


Figure 9. The AA angular correlation scale (asterisks) measured during the night of 2005 July 17 with the UH 0.6-m telescope. This scale is close to the tilt anisoplanatism (squares) calculated in parallel from the SCIDAR data.

also presented (shown by asterisks). This shows good agreement between these two quantities. The tilt anisoplanatism angle gives the maximal distance over which a natural guide star should be used to solve the tilt indeterminism problem inherent in laser guide star adaptive optics systems (Foy et al. 1995).

The comparison between the outer scale measured by the GSM and the integrated MOSP outer scale is appropriate, seeing that both consider the same ν K model of turbulence. Fig. 10 presents comparisons obtained at the OHP where the GSM and MOSP instruments were placed at the same place, 1 m apart. Good agreement is found between these simultaneous measurements.

5 DISCUSSION AND CONCLUSION

The design, performance and optimization of adaptive optics systems are related to considerations of atmospheric turbulence and

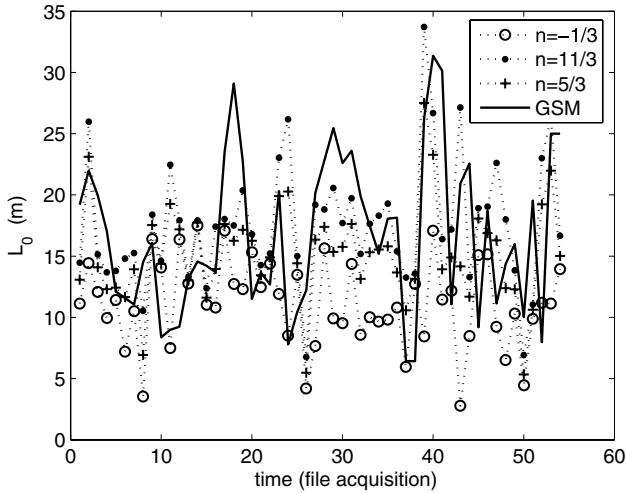


Figure 10. Integrated outer scales (dotted line) deduced from outer scale profiles compared with GSM outer scales (solid line) obtained at the OHP on 2004 November 23, 24 and 28. The parameter n (equation A4), which occurs in the integration of the outer scale profile, depends on the atmospheric conditions and instrumental configuration. Because of irregular time intervals between acquisitions, these time series are ordered by successive acquisitions.

notably to the amplitude of the wavefront outer scale. Several analyses of the effects of the outer scale in terms of the Zernike decomposition of the atmospherically induced phase aberrations have been studied theoretically (Winker 1991; Sasiela & Shelton 1993; Voitsekovich & Cuevas 1995; Conan 2000). Ragazzoni, Le Roux & Arcidiacono (2005) noted that tip-tilt aberrations for ELTs can be corrected with the same mirror used to correct higher-order modes.

Zernike phase variances using outer scale profiles and an integrated outer scale exhibit differences for the tip-tilt modes but no significant differences for higher-order modes. Fig. 11 represents the piston-removed phase variance due to the first 20 Zernike modes calculated with the method described by Winker (1991) with $\lambda = 0.5 \mu\text{m}$. These variances are normalized by the factor $(D/r_0)^{-5/3}$,

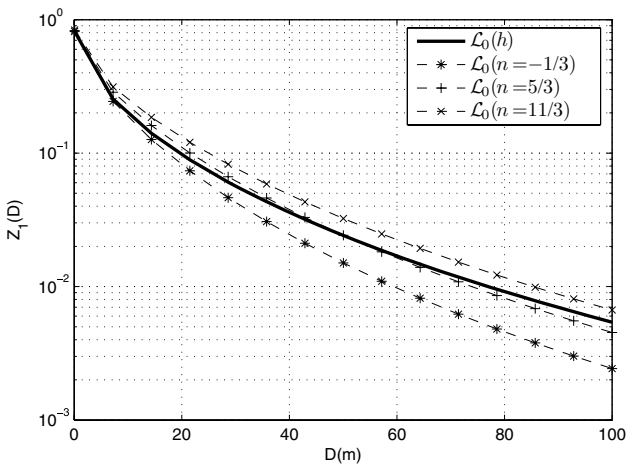


Figure 11. Normalized residual piston-removed phase variance as a function of the telescope diameter. A significant difference occurs when considering the height-dependent outer scale (solid line) instead of the integrated outer scale with $n = -1/3$ (dashed line with asterisks), $n = 5/3$ (plus signs) and $n = 11/3$ (crosses).

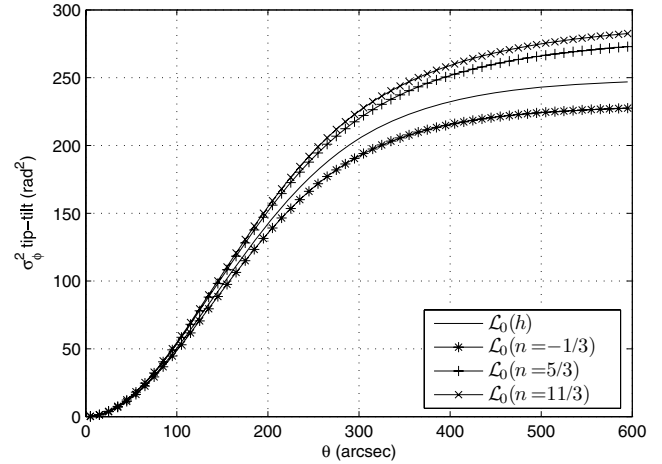


Figure 12. The phase variance due to tip-tilt versus angular separation for a 15-m telescope deduced from the height-dependent outer scale (solid line) measured at Mauna Kea and with an integrated outer scale calculated with $n = -1/3$ (asterisks), $n = 5/3$ (plus signs) and $n = 11/3$ (crosses).

which explains the decrease of the curves when the diameter increases. We use mean $C_N^2(h)$ and median L_0 profiles measured on 2005 July 17 at Mauna Kea (see Section 4) to calculate all the following quantities. If the errors are assumed to be solely the result of atmospheric aberrations, the resulting difference in the Strehl ratio is about 1.5 per cent for $D = 8 \text{ m}$ between the Strehl ratio obtained with outer scale profiles and an integrated outer scale ($n = -1/3$) with $\lambda = 0.5 \mu\text{m}$ and the tip-tilt being compensated.

The use of laser beacons to create artificial reference stars yields the tip-tilt indetermination problem. A natural guide star within the tilt isoplanatism patch is a solution to obtain an optimal correction but limits the sky coverage. The angular distance between the object of the observation and the tip-tilt reference star introduces an error in the correction of the wavefront distortions. Fig. 12 represents phase variances as a result of tip-tilt modes with respect to the angular separation deduced from the analytical expression found by Sasiela & Shelton (1993) and calculated for a 15-m telescope with $\lambda = 0.5 \mu\text{m}$. It is shown that a significant difference occurs when considering the height-dependent outer scale instead of the integrated outer scale.

Observations of the Moon's limb using a straightforward device and small telescope apertures have allowed us to extract profiles of the wavefront outer scale and can be used to obtain a low vertical resolution of C_N^2 profiles. The outer scale profiles estimated during our observations exhibit smaller values in the boundary layer than in the free atmosphere. Comparisons with outer scale measurements using the GSM are possible and give good agreement. High angular resolution techniques could be optimized by considering the height dependence of the outer scale.

ACKNOWLEDGMENTS

We gratefully acknowledge J. Vernin for supplying the SCIDAR data. We are grateful to M. Chun (University of Hawaii) who organized and coordinated the observations in Mauna Kea. Thanks are due to H. Trinquet and A. Berdja for their part in the successful SCIDAR and GSM observations. We also thank H. Lantéri for helpful comments.

REFERENCES

- Aarts E., Korst J., 1989, *Simulated Annealing and Boltzmann Machines*. Wiley, Chichester
- Avila R., Ziad A., Borgnino J., Martin F., Agabi A., Tokovinin A., 1997, *J. Opt. Soc. Am. A*, 14, 3070
- Beckers J. M., 1988, in Ulrich M.-H., ed., *Proc. ESO Conf., Very Large Telescopes and their Instrumentation*. European Southern Observatory, Garching, p. 693
- Belen'kii M. S., 2000, *Appl. Opt.*, 39, 6097
- Borgnino J., 1990, *Appl. Opt.*, 29, 1863
- Borgnino J., Martin F., Ziad A., 1992, *Opt. Commun.*, 91, 267
- Bouziid A., Irbah A., Borgnino J., Lantéri H., 2002, in Vernin J., Benkhalidoun Z., Muñoz-Tuñón C., eds, *ASP Conf. Ser. Vol. 266, Astronomical Site Evaluation in the Visible and Radio Range*. Astron. Soc. Pac., San Francisco, p. 64
- Conan R., 2000, PhD thesis, Univ. Nice Sophia-Antipolis
- Conan R., Ziad A., Borgnino J., Martin F., Tokovinin A. A., 2000a, in Lena P. J., Quirrenbach A., eds, *Interferometry in Optical Astronomy*. Proc. SPIE, 4006, 963
- Conan R., Borgnino J., Ziad A., Martin F., 2000b, *J. Opt. Soc. Am. A*, 17, 1807
- Foy R., Migus A., Biraben F., Grynberg G., McCullough P. R., Tallon M., 1995, *A&AS*, 111, 569
- Frieden B. R., 1983, *Probability, Statistical Optics, and Data Testing*. Springer, Berlin
- Fuchs A., Tallon M., Vernin J., 1998, *PASP*, 110, 86
- Fusco T. et al., 2004, *J. Opt. A: Pure Appl. Opt.*, 6, 585
- Ghedina A., Ragazzoni R., Baruffolo A., 1998, *A&AS*, 130, 561
- Habib A., Vernin J., Benkhalidoun Z., Lanteri H., 2006, *MNRAS*, 368, 1456
- Hardy J. W., 1998, *Adaptive Optics for Astronomical Telescopes*. Oxford Univ. Press, New York
- Ishimaru A., 1978, *Wave Propagation and Scattering in Random Media II*. Academic Press, New York
- Kirkpatrick S., Gelatt C. D., Vecchi M. P., 1983, *Sci*, 220, 671
- Korff D., 1973, *J. Opt. Soc. Am. A*, 63, 971
- Maire J., Ziad A., Borgnino J., Mourard D., Martin F., Jankov S., Bonneau D., Patru F., 2006, *A&A*, 448, 1225
- Martin F., Tokovinin A., Agabi A., Borgnino J., Ziad A., 1994, *A&AS*, 108, 173
- Pratt W. K., 1978, *Digital Image Processing*. Wiley-Interscience, New York
- Ragazzoni R., Marchetti E., Valente G., 2000, *Nat*, 403, 54
- Ragazzoni R., Le Roux B., Arcidiacono C., 2005, *C. R. Physique*, 6, 1081
- Rigaut F., Rousset G., Kern P., Fontanella J. C., Gaffard J. P., Merkle F., Léna P., 1991, *A&A*, 250, 280
- Roddier F., 1981, *Progress in Optics*, Vol. 19. North-Holland, Amsterdam, pp. 281–376
- Roddier F., Cowie L., Graves J. E., Songaila A., McKenna D., 1990, *Advanced Technology Optical Telescopes IV*. Proc. SPIE, 485–491
- Sasiela R. J., Shelton J. D., 1993, *J. Opt. Soc. Am. A*, 10, 646
- Schöck M., Le Mignant D., Chanan G. A., Wizinowich P. L., van Dam M. A., 2003, *Appl. Opt.*, 42, 3705
- Tokovinin A., 2002, *PASP*, 114, 1156
- van Laarhoven P. J. M., Aarts E., 1987, *Simulated Annealing: Theory and Applications*. Kluwer Academic, Dordrecht
- Vernin J., Roddier F., 1973, *J. Opt. Soc. Am.*, 63, 270
- Voitsekovich V. V., 1995, *J. Opt. Soc. Am. A*, 12, 1346
- Voitsekovich V. V., Cuevas S., 1995, *J. Opt. Soc. Am. A*, 12, 2523
- Voitsekovich V. V., Orlov V. G., Cuevas S., Avila R., 1998, *A&AS*, 133, 427
- Winker D. M., 1991, *J. Opt. Soc. Am. A*, 8, 1568
- Ziad A., Conan R., Tokovinin A., Martin F., Borgnino J., 2000, *Appl. Opt.*, 39, 5415
- Ziad A., Schöck M., Chanan G. A., Troy M., Dekany R., Lane B. F., Borgnino J., Martin F., 2004, *Appl. Opt.*, 43, 2316

APPENDIX A:

It will be helpful to compare the values of the outer scale found using methods that consider the outer scale height-independent as measured by the GSM instrument and height-dependent [$\mathcal{L}_0(h)$] as estimated in this paper observing deformations of the Moon's limb. Within the small perturbation approximation, fluctuations produced at ground level by several turbulent layers add linearly (Roddier 1981) and their power spectra as well. Indeed, the total power spectrum is given by $W(f) = \sum_h W(f, h)$, where Fresnel propagation is not taken into account. In the case of the Kolmogorov model of turbulence, the resulting power spectrum at ground level is described using the same model with an optical strength that is the sum of C_N^2 for each altitude. However, the sum of height-dependent vK spectra are not a vK spectrum, except in the case where the outer scale is constant with height. This remark can be generalized to other usual models described, for example, by Voitsekovich (1995).

Let us consider models of observable wavefront quantities as the product of the corresponding vK spectrum by filtering functions with spectral passband range depending on experimental conditions (measured observables, aperture diameter, baselines used, etc.). As a limited portion of the vK spectrum is transmitted, it is possible to find approximative relations that relate the outer scale found with a single-layer whole atmospheric approach to a multilayer description of the atmosphere. Indeed, using the generalized binomial formula to develop the vK spectrum (equation 1) yields

$$W(f)_{f \leq (1/\mathcal{L}_0)} = \epsilon(h) \sum_{k=0}^{+\infty} \left[\begin{matrix} -(11/6) \\ k \end{matrix} \right] f^{2k} \mathcal{L}_0^{(11/3)+2k} \quad (\text{A1})$$

and

$$W(f)_{f \geq (1/\mathcal{L}_0)} = \epsilon(h) \sum_{k=0}^{+\infty} \left[\begin{matrix} -(11/6) \\ k \end{matrix} \right] f^{-(11/3)-2k} \mathcal{L}_0^{-2k} \quad (\text{A2})$$

where

$$\left[\begin{matrix} -(11/6) \\ k \end{matrix} \right] = \frac{-(11/6)[-(11/6)-1] \cdots [-(11/6)-k+1]}{k!}$$

is the binomial coefficient and $\epsilon(h) = 0.38\lambda^{-2} C_N^2(h) \delta h$. If several layers are considered, it gives for spatial frequencies $f \leq \inf\{1/\mathcal{L}_0(h_i)\}_i$ the exact relation for the total power spectrum:

$$W(f) = \sum_{k=0}^{+\infty} \left[\begin{matrix} -(11/6) \\ k \end{matrix} \right] f^{2k} \sum_h \epsilon(h) \mathcal{L}_0(h)^{(11/3)+2k}. \quad (\text{A3})$$

A first-order expansion of this equation gives

$$\mathcal{L}_0 \approx \left[\frac{\sum_h \delta h C_N^2(h) \mathcal{L}_0(h)^n}{\sum_h \delta h C_N^2(h)} \right]^{(1/n)} \quad (\text{A4})$$

with $n = 11/3$. When δh tends to zero, this relation can be extrapolated in a continuous integral form on height h . When outer scales are deduced from observable wavefront quantities, equation (A4) with $n = 11/3$ is appropriate for low-pass filtering functions. For spatial frequencies $f \geq \sup\{1/\mathcal{L}_0(h_i)\}_i$ (equation A2), the resulting spectrum is described well by the Kolmogorov model. For intermediate frequencies of the total spectrum, the relation between outer scales depends on the values of $C_N^2(h)$ and $\mathcal{L}_0(h)$. For large telescopes, or long baseline instruments, the low-frequency part of the spectrum is preponderant in the integral calculus of wavefront quantities. The aperture filter function G (equation 2) cancels out higher frequencies as the aperture increases and the function f (equation 2) is a high-pass filter. Fig. A1 represents AA power spectra for two layers

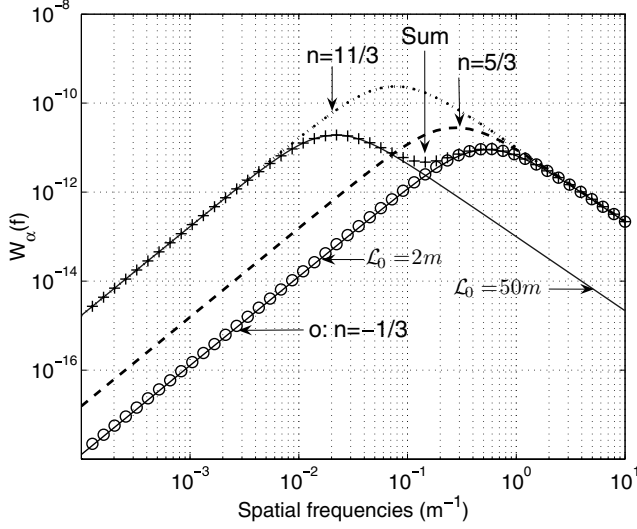


Figure A1. The theoretical sum (shown by plus signs) of two height-dependent AA power spectra (solid lines) for outer scales of 2 and 50 m. The sum is fitted by vK spectra with outer scales calculated using equation (A4) for several values of n . This parameter links the profiles of the wavefront outer scale to the integrated value of the outer scale. The parameter n , which occurs in the integration of the outer scale profile, depends on atmospheric conditions and the instrumental configuration. The best fit of the spectra sum and the corresponding value of n depends on the spatial frequency passband range of the filter functions that multiply the spectra.

with outer scales $\mathcal{L}_0(h_1) = 50$ m, $\mathcal{L}_0(h_2) = 2$ m and $\epsilon(h_2)/\epsilon(h_1) = 100$. Their sum (shown by plus signs) exhibits a non-vK behaviour accentuated by the extreme outer scales chosen. In the case considered in Fig. A1, intermediate frequencies are predominant when the power spectra are integrated.

The phase structure function is often used in the statistical description of wavefront aberrations. Conan et al. (2000a) found three asymptotic formulations of the phase structure function averaged over circular apertures with baseline B , as follows.

(i) $D \ll B \ll \mathcal{L}_0/\pi$:

$$D_\phi^{vK}(\mathbf{B}) = 6.88 \left(\frac{B}{r_0}\right)^{5/3} \left[1 - 1.49 \left(\frac{B}{\mathcal{L}_0}\right)^{1/3}\right].$$

(ii) $D \ll \mathcal{L}_0/\pi \ll B$:

$$D_\phi^{vK}(\mathbf{B}) = 0.17 \left(\frac{\mathcal{L}_0}{r_0}\right)^{5/3}. \quad (\text{A5})$$

(iii) $\mathcal{L}_0/\pi \ll D \ll B$:

$$D_\phi^{vK}(\mathbf{B}) = 0.06 \left(\frac{D}{r_0}\right)^{5/3} \left(\frac{D}{\mathcal{L}_0}\right)^{-11/3}.$$

If we consider these valid for each altitude h and substitute equation (3) into equation (A5), we have the following.

(i) $D \ll B \ll \mathcal{L}_0(h)/\pi$:

$$D_\phi^{vK}(\mathbf{B}, h) = 2.91 \left(\frac{2\pi}{\lambda}\right)^2 C_n^2(h) \delta h B^{5/3} \times \left[1 - 1.49 \left(\frac{B}{\mathcal{L}_0(h)}\right)^{1/3}\right].$$

(ii) $D \ll \mathcal{L}_0(h)/\pi \ll B$:

$$D_\phi^{vK}(\mathbf{B}, h) = 0.072 \left(\frac{2\pi}{\lambda}\right)^2 C_n^2(h) \delta h \mathcal{L}_0(h)^{5/3}. \quad (\text{A6})$$

(iii) $\mathcal{L}_0(h)/\pi \ll D \ll B$:

$$D_\phi^{vK}(\mathbf{B}, h) = 0.025 \left(\frac{2\pi}{\lambda}\right)^2 C_n^2(h) \delta h \frac{1}{D^2} \mathcal{L}_0(h)^{11/3}.$$

In the first case, when $D \ll B \ll \mathcal{L}_0(h)/\pi$ for all h , equation (A4) is found with $n = -1/3$. This relation was found first by Borgnino (1990). It is appropriate for high values of the outer scale (i.e. when stronger layers are well described by the Kolmogorov model and for average over small apertures).

When $\mathcal{L}_0(h)/\pi \ll D \ll B$ for all h , the total phase structure function deduced from item (iii) of equation (A6) yields equation (A4) with $n = 11/3$. This relation is appropriate, for example, for large apertures as ELTs.

When $D \ll \mathcal{L}_0(h)/\pi \ll B$ for all h is verified, the total phase structure function is given by equation (A4) with $n = 5/3$. The different regimes of equation (A6) imply that the relation between the vertical profiles of the outer scale and the ‘single layer’ outer scale depends on experimental conditions. Fig. 13 shows how the AA power spectra obtained with these three different outer scale relations fit the sum of the two-layer spectra. The integrand of the structure function (equation 2) is well fitted depending on the spatial frequency passband range of the filter functions as a result of experimental configurations and atmospheric conditions.

This paper has been typeset from a $\text{\TeX}/\text{\LaTeX}$ file prepared by the author.